Mechanical Engineering Faculty Publications and Presentations

College of Engineering and Computer Science

2-21-2019

Linear stability analysis of subaqueous bedforms using direct numerical simulations

Nadim Zgheib

S. Balachandar

LINEAR STABILITY ANALYSIS OF SUBAQUEOUS BEDFORMS USING DIRECT NUMERICAL SIMULATIONS

N. Zgheib[1,2]† and S. Balachandar[2]

[1]*School of Engineering, Lebanese American University, Byblos, Lebanon*

[2]*Department of Mechanical and Aerospace Engineering, University of Florida, Gainesville, FL 32611, USA*

Abstract

We present results on the formation of ripples from linear stability analysis. The analysis is coupled with direct numerical simulations of turbulent open channel flow over a fixed sinusoidal bed. The presence of the sediment bed is accounted for using the immersed boundary method. The simulations are used to extract the bed shear stress and consequently the sediment transport rate. The approach is different from traditional linear stability analysis in the sense that the phase lag between the bed topology and the sediment flux is obtained from the three-dimensional turbulent simulations. The stability analysis is performed on the Exner equation, whose input, the sediment flux, is provided from the simulations. We ran 11 simulations at a fixed shear Reynolds number of 180, but for different sediment bed wavelengths. The analysis allows us to sweep a large range of physical and modelling parameters to predict their effects on linear growth. The Froude number appears to be the critical controlling parameter in the early linear development of ripples, in contrast with the dominant role of particle Reynolds number during the equilibrium stage. We also present results from a wave packet analysis using a one-dimensional Gaussian ridge.

† Correspondence to: nadim.zgheib@lau.edu.lb

1. Introduction

Ripples are examples of bedform patterns that result from the instability of an erodible bed of particles subjected to the shearing action of an overlying flow field. They are present in Aeolian (e.g. Andreotti et al. 2006) and subaqeous (e.g. Baas 1994) environments, and have been even observed on the surface of other planets (e.g. Sivestro et al. 2010). They may evolve from a completely flat bed and their evolution depends on the flow and particle properties (e.g. Kennedy 1969). While their formation has been mostly studied under turbulent flow field conditions (e.g. Blondeaux 1990), they are also known to form under laminar flows (e.g. Coleman & Eling 2000, Ouriemi et al. 2009).

Before reaching an equilibrium state, ripples go through multiple stages as they evolve from an initially flattened bed (e.g. Perillo et al. 2014). Based on a series of flume experiments, Coleman & Melville (1996) observed ripples to be first instigated by the occurrence of small sediment pileups. These pileups quickly straighten to become locally two-dimensional and interact with the overlying flow field to generate further pileups at a downstream location. These newly formed pileups, through the same mechanisms that lead to their formation, in turn generate additional pileups further downstream. The induced pileups do not form at random downstream locations, but rather at some preferred spacing from the parent pileup. Coleman & Melville (1996) found this preferred spacing to be weakly dependent on flow conditions and to scale with particle diameter. However, as noted by Langlois & Valance (2007), this grain size-dependence on the preferred spacing should be taken with caution due to the large dispersion in the data.

Two main approaches have been principally used to extract the dependence of this preferred spacing (or initial wavelength of emerging ripples) on flow and bed parameters. The first is

2

through laboratory experiments (e.g. Baas 1994, 1999, Coleman & Melville 1994, 1996, Rauen et al. 2008, Perillo et al. 2014), while the second is through a mathematical/theoretical approach, primarily by means of linear stability analysis (e.g. Kennedy 1969, Jain and Kennedy 1974, Richards 1980, Charru & Mouilleron-Arnould 2002, Ouriemi et al. 2009b, Fourriere et al. 2010, Camporeale & Ridolfi 2011, Colombini & Stocchino 2011,Bohorquez & Ancey 2015, Caruso et al. 2016). In the case of laboratory experiments, capturing the wavelength of ripples can be quite challenging for the following reasons: (i) The amplitude of incipient ripples, at the earliest stages of formation, can be very small of the order of a few grains. This requires a measuring device with very fine resolution. This is further exacerbated by the rough nature of the particle bed (Langlois & Valance 2007). (ii) Owing to the fact that the developing ripples are continuously coarsening over time (e.g. Robert & Uhlman 2001, Venditti et al. 2005), the wavelength measurements need to be made within a small time window to truly capture the wavelength at the very early stages. If averaged over long enough times, measurements are likely to overestimate the wavelength of initial development. (iii) Owing to the inherent nature of the problem, the bed measurements need to be made over a relatively wide area spanning multiple wavelengths, which requires a finite time to execute. It is for this reason that the bed is often temporarily "frozen" during these measurements by reducing (or completely shutting down) the overlying fluid flow rate such that the shear velocity at the bed is well below the critical shear velocity needed for incipient motion (e.g. Nakagawa & Tsujimoto 1984). The bed is then "unfrozen" after the measurements by ramping up the fluid flow rate to its previous value. This freezing and unfreezing of the bed could affect the natural progression of bedform evolution. (iv) In any physical setting, the flow rate cannot instantaneously jump from still conditions to the desired value at which the experiment

is conducted. This poses an inconvenience when trying to extract the dependence of the initial wavelength on flow parameters, as incipient particle motion is likely to occur before the flow reaches its target value. It could then become difficult to associate the observed incipient wavelength with the correct fluid flow conditions.

As for the linear stability analysis, it has its weaknesses; (i) most importantly, processes that occur on the grain-scale, in terms of grain motion in response to the hydrodynamic forces acting on it, are modelled in terms of an empirical correlation for the bedload. As a result, the accuracy of the predictions of the stability analysis are dependent on the fidelity of the bedload transport model. (ii) Furthermore, idealizations such as spanwise periodicity often employed in the stability analysis are not applicable both under field conditions are even in the controlled laboratory experiments. Such differences must be factored when comparing the predictions of the stability analysis against corresponding experiments. (iii) Finally, linear (and subsequent weakly-nonlinear) stability analysis are useful only in explaining the early stages of bed evolution.

The linear stability approach is rooted in the fact that many scientists agree that ripples develop as a result of instability (e.g. Richards 1980, McLean 1990). This instability is associated with a positive phase shift between the sediment transport rate and the bed elevation (e.g. Engelund & Fredsoe 1982, Bridge & Best 1988,). That is, if the bed height elevation, which is initially flattened, is perturbed sinusoidally, then the maximum sediment transport rate does not occur at the crest, but rather slightly upstream. This phase shift is necessary for carrying out the stability analysis and knowing its correct value is crucial for the accuracy of the results (e.g. Bennett & Best 1995). The phase shift depends on a variety of factors pertaining to the fluid flow and sediment bed. Perhaps the most important factor, according to Engelund & Fredsoe (1982) is the bed shear

velocity. However, computing the phase shift from governing laws of fluid motion and sediment transport can be challenging.

The purpose of the present work is to conduct a linear stability analysis in conjunction with direct numerical simulations (DNS) of flow over a non-erodible wavy bed (Zilker et al. 1977, Hudson et al. 1996, Cherukat et al. 1998, Calhoun & Street 2001). This approach is different from the classical linear stability analysis in the sense that the DNS naturally provide the phase shift between the bed shear stress and the bed topology. The Meyer-Peter & Müller (1948) relationship is then used to extract the sediment flux from the bed shear stress, and with it the phase lag between the sediment flux and the bed topology. Once the phase lag is known, each simulation can be used to test for the effects of a variety of parameters on the wavelength of the developing ripples.

This paper is arranged as follows. In Section 2, we discuss the mathematical model and more specifically the use of the immersed boundary method to account for the presence of the sediment bed. In Section 3, we elaborate on the linear stability analysis and show that it can, in the present context, reproduce the wavelength observed in coupled, time-evolving bed-flow simulations. We then sweep the parameter space and investigate the effects of a variety of physical and modelling parameters in Section 3.3. We further conduct a wave packet analysis by studying the evolution of a small amplitude Gaussian ridge in Section 4. Conclusions are drawn in Section 5.

2. Mathematical model
The physical problem that is being modelled in this study corresponds to a pressure-driven unidirectional turbulent flow over a fixed (or for certain cases erodible) bed of sediment particles.

In the case of an erodible bed, flow parameters and particle properties are chosen such that the dominant mode of transport is bedload with no to little particle saltation or resuspension. Bedload-dominated particle transport is usually observed when the flow shear velocity at the bed is marginally in excess of the critical shear velocity required for incipient motion of particles. We should note at this point that while we resolve large and small-scale flow features such as those in the turbulent eddies in Figure 2a, we do not explicitly consider the effects of individual particles on the flow field , but rather the collective action of a group of particles. In other words, the bed evolution (when the bed is erodible) and the coupling between the bed and the flow are investigated at the mesoscale level.

The present setup is different from particle-resolved simulations (Kidanemariam & Uhlmann 2014, 2017) in which flow around individual particles is resolved. There, the setup necessitates a sub-grain resolution for which the grid must be sufficiently smaller than individual particles or grains. These simulations can be computationally very expensive, as they require very fine resolution and a correspondingly small enough time step. Another approach has been to resolve the mesoscale turbulence while tracking individual grains as Lagrangian particles and allow them to interact using discrete element (DEM) approach (Apte et al. 2008,, Nabi et al. 2013; Sun & Xiao 2016). This approach has the advantage of not needing a bedload transport model. However, instead it requires the use of hydrodynamic drag/lift laws and inter-granular contact/collision models. As an alternative to the aforementioned fully-resolved and DEM simulations, the flow may be resolved using large-eddy or direct numerical simulations, while the evolution of the bed may be modelled at the mesoscale using the Exner equation (Chou & Fringer 2010, Escauriaza & Sotiropoulos 2011, Khosronejad et al., 2011, Sotiropoulos & Khosronejad 2016). We employ the

latter approach in the present study where we utilize a grid that is sufficiently fine to resolve the smallest Kolmogorov flow scales, but coarse enough to encompass a number of particles within a cell volume.

The numerical setup consists of a rectangular domain as shown in (Figure 1). Fourier expansions are used along the x (streamwise) and y (spanwise) directions, which require the use of periodic boundary conditions. Chebyshev polynomials are used in the vertical z direction with free-slip boundary condition at the top of the computational domain. The presence of the immersed boundary (shown as a shaded flat plane in Figure 1) above the lower boundary of the rectangular domain (see inset of Figure 1) renders the actual boundary condition applied at the bottom of the computational domain to be not important, since the immersed boundary represents the effective lower boundary of the flow. However, since boundary conditions must be imposed at all the boundaries of the numerical domain, a zero velocity condition is imposed at the lower boundary. We should stress however that the details of this boundary condition are not important as reasoned above.

A constant mean pressure gradient along the x-direction drives the flow. No pressure gradient is imposed along the spanwise y-direction, and as a result no mean flow exists along that direction (only perturbation flow is present). The presence of the fixed (or mobile) bed is accounted for using the direct forcing immersed boundary method (IBM) of Uhlmann (2005). More details about the method can be found in Uhlmann (2005), Akiki & Balachandar (2016), and more recently in Zgheib et al. (2018a,b). Only a brief description of the method is provided at the end of this section for completeness.

We start first with a brief description of the governing equations. These consist of conservation of mass (1) and momentum (2). These conservation equations are integrated using a pseudo spectral code (Cortese & Balachandar 1995, Cantero et al. 2007, Shringarpure et al. 2012). If the bed is allowed to evolve, the Exner equation (3) (Cayocca 2001, Paola & Voller 2005, Ancey 2010) is used to update its position. On the other hand, when the bed is held fixed, only equations (1) and (2) are integrated. The volumetric flux of particles $\boldsymbol{q}$, which represents the input to the Exner equation, is obtained from the flow-induced shear stress at the bottom boundary of the fluid domain as defined by the bed. The non-dimensional governing equations for the flow and the bed are shown below

$$\nabla \cdot \boldsymbol{u} = 0 , \tag{1}$$

$$\frac{D\boldsymbol{u}}{Dt} = \boldsymbol{e}_x - \nabla p + \frac{1}{Re_\tau}\nabla^2 \boldsymbol{u} + \boldsymbol{f}, \tag{2}$$

$$\varphi \frac{\partial \eta}{\partial t} = -\nabla \cdot \boldsymbol{q} + \varepsilon \langle |\boldsymbol{q}| \rangle \nabla^2 \eta, \tag{3}$$

In (1) and (2), $\boldsymbol{u}$ represents the three components of the velocity field. $\boldsymbol{e}_x$ is a unit vector in the x-direction and here represents the non-dimensional mean pressure gradient. p corresponds to the perturbation pressure due to turbulent fluctuations, and Re_τ is the shear Reynolds number defined using the velocity and length scales as

$$Re_\tau = \frac{U_\tau^* H_f^*}{\nu^*}, \tag{4}$$

The velocity scale U_τ^* is the average shear velocity on the bed, and the corresponding pressure scale $\rho_f^* U_\tau^{*2}$ results in a non-dimensional streamwise pressure gradient of unity, where ρ_f^* is the fluid density. H_f^* corresponds to the mean flow depth, and ν^* is the kinematic viscosity of the

fluid. The ratio H_f^*/U_τ^* represents the time scale. The last term on the right hand side of (2), the IBM coupling force f, is the force that is imposed on the immersed boundary to ensure the no-slip and no-penetration conditions are satisfied at the bed. Here f is defined as

$$f(x) = \sum_{i=1}^{N_i} F(X_i)\delta(x - X_i)\Delta V_i, \tag{5}$$

where $F(X_i)$ is the force applied at the ith Lagrangian marker to enforce the no-slip and no-penetration condition, $\delta(x - X_i)$ is the discrete delta function used to ensure that the force on the ith Lagrangian marker only spreads over a few Eulerian grid points surrounding that marker (Akiki & Balachandar 2016), and ΔV_i denotes the volumetric weight of the ith marker taken here as the product of the grid spacings around the ith marker. N_i corresponds to the total number of Lagrangian markers.

Throughout the manuscript, the asterisk denotes a dimensional quantity, while all other parameters are to be treated as non-dimensional with respect to the aforementioned scales.

As for the Exner equation (3), it describes the evolution of an erodible bed subjected to a shearing flow. The first term represents the time rate of change of the bed elevation η, where $\varphi = 0.6$ corresponds to the volume fraction of the sediment bed under close-packing conditions, and $\varepsilon = 4$ is an adjustable parameter (Cayocca 2001) that controls the numerical diffusion term.

A total of 11 fixed-bed simulations were performed, the details of which are shown in Table 1. The present resolution of $288 \times 96 \times 301$ grid points along the streamwise, spanwise, and vertical directions was chosen to match recent studies by Zgheib et al (2018a,b) for $Re_\tau = 180$. The immersed boundary, which describes the surface of the sediment bed, has the same x-y

9

resolution as the flow with $N_x \times N_y$ Lagrangian markers. Additionally, the x and y positions of these markers overlap with the underlying Eulerian grid, whereas the vertical position of the bed (i.e. the immersed boundary) does not coincide with the Eulerian grid. We should note that the flow is fully turbulent at the selected shear Reynolds number of $Re_\tau = 180$ (Kim et al. 1987, Zgheib et al. 2018b).

We now provide a brief overview on the implementation of the immersed boundary method, with more details available in Akiki & Balachandar (2016) and Zgheib et al. (2018a). We define two separate grids. The first is the Eulerian grid, which consists of $N_x \times N_y \times N_z$ grid points (see Table 3). It is at those grid points that the velocity components and pressure are defined and temporally updated through the continuity and Navier-Stokes equations. The Eulerian grid points are fixed and thus the location of the grid points remain unchanged with time. The second grid, which is detached from the Eulerian grid, is termed the Lagrangian grid. This grid consists of $N_x \times N_y$ grid points termed markers. It is these markers that make up a surface which defines the sediment bed. The x and y locations of these markers do not change with time and coincide with the x and y locations of the Eulerian grid. However, the vertical coordinate of the markers vary with time (for the case of an erodible sediment bed) or remain fixed (in the case of a non-erodible sediment bed). In any case, the vertical coordinate of the markers will not generally match the location of the vertical coordinate of the Eulerian grid. The purpose of the IBM is to impose a specific set of conditions on the flow at the location of these Lagrangian markers. In the present simulations, the IBM serves to enforce the no-slip and no-penetration conditions to simulate the presence of a sediment bed. In other words, the flow velocity is forced to zero at the sediment bed. This is achieved by first computing the velocity at each of the $N_x \times N_y$

Lagrangian markers. This velocity is computed through interpolation from the velocity of the adjacent Eulerian grid. Only the nearest three Eulerian grid points along the x, y, and z directions are considered in the interpolation process, so that the total number of Eulerian grid points involved in the interpolation process is 9 . We note here that the velocity at the Eulerian grid points is weighted by the local Eulerian grid volume $\Delta x \times \Delta y \times \Delta z$, the product of the grid spacing along the three directions. The velocity at each marker is then set to the desired value (zero velocity in the present context) by applying a force that is proportional to the difference between the desired and actual (interpolated) value at each marker. It is this force that is then spread back onto the surrounding Eulerian grid to achieve the aforementioned desired set of conditions. The spreading operation involves a discrete delta function to ensure that the aforementioned force only applies to the nearest Eulerian grid points. Here again, the weight of each Lagrangian marker is given by the local grid volume $\Delta x \times \Delta y \times \Delta z$.

We should note here that the physical problem of pattern formation under a shearing turbulent channel flow contains a variety of time scales. These include hydrodynamic and bedform deformation time scales. The time scales can be represented as a ratio of a length scale to a velocity scale. For the hydrodynamic time scale, the bulk velocity may be chosen as the velocity scale, whereas the grid spacing (in lieu of the Kolmogorov length scale) and the domain's height may be used as length scales. Therefore, the slow hydrodynamic time scale becomes the ratio of the height of the computational domain to the bulk velocity. On the other hand, we may define the fast hydrodynamic time scale as the ratio of the grid size to the bulk velocity. As for the bedform deformation time scales, we may use the shear velocity as the characteristic velocity scale and the wavelength of the bedform as the characteristic length scale. Their ratio would

define the slow bedform deformation scale. Alternatively, if we were to use the grain diameter as the length scale, then the fast bedform deformation scale becomes the ratio of the particle diameter to the shear velocity.

Table 2 summarizes the aforementioned time scales. We should note here however, that because in the present linear stability analysis the bed is held fixed, it follows that the bedform deformation scales are no longer applicable and the problem reduces to an open turbulent channel flow over a sinusoidal bed, where only the hydrodynamic scales are active.

3. Linear stability of the Exner equation using direct numerical simulations

The fluid flow over an erodible bed of particles, may under certain conditions, work (or modify) the shape of the underlying erodible bed over which it flows. In fact, when the flow intensity is strong, or more specifically, when the flow-induced bed shear stress is above some threshold value, the bed topology will be modified by the flow. The Shields diagram (Shields 1936) provides a practical means for predicting the aforementioned threshold value under various flow conditions and particle properties. Additionally, we may distinguish two flow regimes when the shearing flow is strong enough to displace particles and modify the bed. The first regime corresponds to the case when the flow is very vigorous such that particle transport occurs through resuspension and saltation in addition to bedload (e.g. Engelund 1970). On the other hand, when the flow parameters are such that the conditions for incipient motion of particles are marginally exceeded, bedload would constitute the dominant mode of transport with little to no saltation or resuspension (e.g. Paarlberg et al. 2009). The latter of the two regimes is the focus of the present study.

Coleman & Melville ([1996](#)) argued that the earliest bedforms that form are instigated by the presence of random pileups within the bed. These pileups straighten and form downstream pileups at some preferred wavelength. The newly formed pileups in turn generate additional pileups further downstream at the same preferred wavelength, and this process repeats until the entire bed is seeded with these incipient bedforms. Zgheib et al. ([2018a](#)) were able to reproduce these early time dynamics as described by Coleman & Melville ([1996](#)) using direct numerical simulations. They found the temporal and spatial evolution of the bed in the vicinity of a sand pileup to resemble the evolution proposed in the theory of Coleman & Melville ([1996](#)). Here we are attempting a different approach using linear stability analysis to study the very early stages of bedform development.

Under turbulent flow conditions, the inception of bedforms from a completely flat bed is a result of the near-bed turbulent structures. Such structures include hairpin vortices and cane-shaped quasi-streamwise vortices which are readily visible in Figure 2a. In fact, these vortices are likely responsible for the emergence of quasi-spanwise streaks which later grow and merge to form the incipient ripples. Figure 2a shows iso-surfaces of the swirling strength $\lambda_{ci} = 15$ in the bottom half of the computational domain. The swirling strength helps to locate the hairpin vortices by identifying regions of intense vortical structures (Zhou et al. 1999, Chakraborty et al. 2005). It is defined as the absolute value of the imaginary portion of the complex eigenvalue of the velocity gradient tensor.

When the bedform amplitudes are very small, such as those used in the present stability analysis, their instantaneous effect on the overlying flow is very subtle. For example, it is not possible to identify the shape of the bed by analyzing the instantaneous vortical structures in Figure 2a or

13

the instantaneous overlying flow field in Figure 2b. This behavior is also evident in the iso-contours of the instantaneous wall shear stress (or alternatively the bed-normal gradient of tangential velocity in panel (c)). We should note that the snapshots in all panels of Figure 2 correspond to the same instance when the flow has reached a stationary state.

On the other hand, once the stationary flow has been time-averaged for a sufficiently long period, the imprint of the bed on the flow becomes apparent (Calhoun & Street 2001). In Figure 3 we plot the time- and span-averaged bed-normal gradient of tangential velocity ($\partial\langle\bar{u}_t\rangle/\partial n$) versus the streamwise coordinate x. Here, $\partial\langle\bar{u}_t\rangle/\partial n = \nabla\langle\bar{u}_t\rangle \cdot \boldsymbol{n}$, where $\langle\bar{u}_t\rangle$ is the streamwise-aligned bed tangential velocity, and $\boldsymbol{n}$ is unit vector pointing in the bed-normal direction. From the streamwise variation of $\partial\langle\bar{u}_t\rangle/\partial n$, we can readily identify the shape of the bed. In fact, $\partial\langle\bar{u}_t\rangle/\partial n$ varies in the same sinuous manner as the bed, but with a positive phase shift. That is, the peak of $\partial\langle\bar{u}_t\rangle/\partial n$ occurs upstream of the corresponding peak of the bed height η (see Figure 3i). It is this phase shift that is crucial for the present linear stability analysis.

3.1   *Fourier decomposition*

We perform a linear stability analysis with a small sinusoidal disturbance to an otherwise flat, non-erodible bed using the Exner equation (3). The prescribed sinusoidal disturbance to the bed is spanwise invariant. However, while the stability analysis is two-dimensional (does not incorporate spanwise dependence), the simulations are fully three-dimensional, since three-dimensionality is essential to sustain wall turbulence. The restriction to two-dimensional perturbations is mainly motivated by the observation of two-dimensional ripples. We note here that even three-dimensional disturbances in the form of Gaussian bumps quickly become two-

dimensional. We will discuss below how we bridge the two-dimensional stability analysis and the fully three-dimensional simulations.

Since the stability analysis is spanwise invariant, we only need to consider a simplified form of the Exner equation with no spanwise dependence, i.e. the 1-D Exner equation

$$\varphi \frac{\partial \eta}{\partial t} + \frac{\partial \bar{q}}{\partial x} - \epsilon \bar{\bar{q}} \frac{\partial^2 \eta}{\partial x^2} = 0 \ . \tag{6}$$

In the above, $\bar{q}$ is the bedload volumetric flux of particles and $\bar{\bar{q}}$ is the mean bedload flux over the entire bed. Here and in the remainder of the manuscript, the two overbars denote spatial averaging along the streamwise (x) and spanwise (y) directions. The mathematical expression is included in Table 3. These quantities are computed using the bed shear stress of the three-dimensional simulations presented in Table 1 as follows. Once the flow reaches a stationary state, it is span and time averaged to yield the corresponding span and time averaged bed shear stress $\langle \overline{\tau^*} \rangle(x)$. $\langle \overline{\tau^*} \rangle(x)$ is then used to compute the average Shields number $\langle \overline{\Theta} \rangle(x)$, which in turn is needed to compute $\bar{q}(x)$ and $\bar{\bar{q}}$. More specifically, as indicated in Table 3, which provides a comprehensive list of the variables used in this study as well as notation and nomenclature, the span and time averaged quantities are expressed as

$$\langle \overline{\Theta} \rangle = \frac{\langle \overline{\tau^*} \rangle}{\left(\rho_p^* - \rho_f^* \right) g^* d_p^*}$$

$$\bar{q} = \frac{Re_p}{Re_\tau} c_1 (\langle \overline{\Theta} \rangle - \Theta_{cr})^{c_2} \tag{7}$$

$$\bar{\bar{q}} = \frac{Re_p}{Re_\tau} c_1 \left(\langle \overline{\overline{\Theta}} \rangle - \Theta_{cr} \right)^{c_2} ,$$

where c_1 and c_2 are parameters of the bedload transport model. Note that while the bed is held fixed in the direct numerical simulations, we are performing the stability analysis to anticipate its early time evolution, and thus η becomes implicitly time dependent in the stability analysis. In a similar fashion, the bedload flux $\bar{q}$ is treated as a time dependent variable in the analysis.

The modified Exner equation in (6) is the only expression needed to carry out the stability analysis. The simulations serve to provide the input to (6) in the form of $\overline{\Theta}$, from which $\bar{q}$ and $\bar{\bar{q}}$ are computed. As such, the stability analysis does not require an "ad-hoc" phase shift between the bed shear stress and the bed topology (e.g., Colombini 2004; Vesipa et al. 2012).

The stability analysis consists of first Fourier expanding $\eta(x, t)$ and $\langle \overline{\Theta} \rangle (x, t)$ up to the first order terms

$$\eta = \eta_0 + \eta_1 e^{\alpha_1 t} e^{\mathrm{i}\frac{2\pi x}{\lambda}} + complex\ conjugate + HOT$$

$$\langle \overline{\Theta} \rangle = \langle \overline{\Theta} \rangle_0 + \langle \overline{\Theta} \rangle_1 e^{\alpha_1 t} e^{\mathrm{i}\frac{2\pi x}{\lambda}} + complex\ conjugate + HOT \ .$$

(8)

In the above, $\eta_0 = 0$ is the mean bed elevation, and $\langle \overline{\Theta} \rangle_0 = \langle \overline{\overline{\Theta}} \rangle$. The coefficients η_1, $\langle \overline{\Theta} \rangle_1$, and α_1 are complex:

$$\eta_1 = \eta_{1R} + i\eta_{1I} \quad ; \quad \langle \overline{\Theta} \rangle_1 = \langle \overline{\Theta} \rangle_{1R} + i\langle \overline{\Theta} \rangle_{1I} \quad ; \quad \alpha_1 = \alpha_{1R} + i\alpha_{1I} \ .$$

(9)

However, since the prescribed sinusoidal disturbance is of the form $\eta = \delta \cos\left(\frac{2\pi x}{\lambda}\right)$ as shown in Figure 4, it follows that η_{1I} is identically zero and $\eta_{1R} = \delta$. As for the Shields number $\langle \overline{\Theta} \rangle_1$, we note that the presence of a non-zero imaginary component indicates a phase shift between the shear stress and the bed topology. We know from previous studies (e.g. Bennett & Best 1995) that such a phase shift is necessary for the bed to be unstable. Finally, the exponential time coefficients, α_{1R} and α_{1I} represent the growth rate and phase speed of the bedform, respectively.

One of the main objectives of the linear stability analysis is to find the growth rate and phase speed of the most amplified mode. That is, we are interested in identifying the wavelength λ in Figure 4, for which α_{1R} is a maximum. Substituting (7), (8) and (9) into (6) and equating terms of the same order, we arrive at a system of two equations with two unknowns α_{1R} and α_{1I}. These may be solved to obtain

$$\alpha_{1R} = \left(\frac{Re_p}{Re_\tau} c_1\big(\langle\bar{\bar{\Theta}}\rangle - \Theta_{cr}\big)^{c_2-1}\right)\frac{2\pi}{\lambda\varphi}\left[c_2 \frac{\langle\bar{\Theta}\rangle_{1I}}{h_{1R}} - \varepsilon\big(\langle\bar{\bar{\Theta}}\rangle - \Theta_{cr}\big)\frac{2\pi}{\lambda}\right]$$

$$\alpha_{1I} = -\frac{Re_p}{Re_\tau} c_1\big(\langle\bar{\bar{\Theta}}\rangle - \Theta_{cr}\big)^{c_2-1} c_2 \frac{2\pi}{\lambda\varphi}\frac{\langle\bar{\Theta}\rangle_{1R}}{h_{1R}} \ .$$

(10)

While the above relations show some explicit dependence on parameters such as Re_τ and Re_p, we should be careful not to assume that the dependence on such parameters is as shown explicitly in (10). For example, as we will show later on, it is true that α_{1R} generally increases with Re_p, however this increase is not necessarily linear. We need to keep in mind that the Shields number (see Table 3) also depends on parameters that affect Re_p such as particle diameter and particle density.

Equation (10) provides some indication on how various parameters affect the stability of the bed. Perhaps the least interesting scenario is that for which $\langle\bar{\bar{\Theta}}\rangle < \Theta_{cr}$ or in other words for which the mean shear stress on the bed is less than the critical shear stress needed for incipient motion. For this case, the bed is immobile and stable. A more interesting setting is for which $\langle\bar{\bar{\Theta}}\rangle > \Theta_{cr}$. For this case the magnitude of the phase speed will increase as the mean Shields number increases above the critical value Θ_{cr}. Also we find the magnitude of the phase speed to be proportional to $\langle\bar{\Theta}\rangle_{1R}$. On the other hand for α_{1R}, we are interested in how the magnitude and sign of this growth coefficient vary. The larger the amplitude, the faster the bed develops and the

sooner the bedform patterns evolve. A positive growth rate indicates that the amplitude grows (unstable setting), while a negative growth rate (stable setting) indicates that any perturbation to the bed would decay over time.

For the case of α_{1R}, the dependence is not as straightforward as for α_{1I}. Here, there are two competing terms which include the excess shear stress term $\langle\overline{\overline{\Theta}}\rangle - \Theta_{cr}$. Depending on the relative magnitude of each term, the outcome may vary. What is certain is that a positive phase shift between the bed topology and bed shear stress (i.e. $\langle\overline{\overline{\Theta}}\rangle_{1I} > 0$) is necessary for the bed to become unstable. If no positive phase shift exists or if the phase shift is very small such that the term in the square brackets in (10) is negative, then $\alpha_{1R} < 0$ and the bed is stable.

The reason a critical positive value of $\langle\overline{\overline{\Theta}}\rangle_{1I}$ is needed for instability is due to the second term within the square parenthesis in the equation for α_{1R}. This term arises from the third term (i.e. the diffusion term) in (6). The purpose of this diffusion term is to supress short wavelength instability. From (10), we observe this diffusion term to be proportional to the diffusion coefficient ε and inversely proportional to the wavelength λ. This means the shorter the wavelength is, the larger the tendency to suppress it.

Because of the implicit and non-linear dependence of α_{1R} and α_{1I} on a variety of factors, it is difficult to anticipate how they will vary from a qualitative examination of (10). We perform a parametric study in Sections 3.3.1 and 3.3.2 to investigate the dependence of α_{1R} and α_{1I} on physical and modelling parameters, respectively.

While the exponential coefficients were obtained through a linear stability analysis of the 1-D Exner equation (6), the simulations in Table 1 were performed for the primary purpose of

obtaining the bed shear stress and consequently the bedload flux. In fact, from the knowledge of near bed turbulence at other Re_τ values (Zilker et al. 1977, Hudson et al. 1996, Cherukat et al. 1998), the stability analysis can be easily reproduced at those Re_τ values.

3.2   *Linear stability analysis for a specific set of parameters*

While the temporally-evolving Gaussian bump simulations presented in Zgheib et al. (2018a) were very useful in dissecting the various stages of evolution depicted in Coleman & Melville's (1996) theory, the simulations are only representative of the specific set of conditions used therein. In the present study, we test the applicability of linear stability analysis in predicting the initial evolution of an erodible bed with the advantage that the same simulation could be used to predict the initial stages of bedform evolution for a wide range of parameters. On the other hand, the stability analysis is only useful for the early linear stages of bed evolution unlike the erodible bed simulations in which the bed and the flow can interact non-linearly and evolve continuously in a complex manner.

In Figure 5, we show a plot of the growth rate and wave speed versus wavelength for two cases with parameters corresponding to two simulations from Zgheib et al. (2018a). Both cases have the same particle Reynolds number $Re_p = 4.34$, but different Froude numbers $Fr_\tau = 0.032$ (panels (a) & (c)) and $Fr_\tau = 0.019$ (panels (b) & (d)). The dashed vertical line in panels (a) and (c) mark the value of the wavelength λ for which α_{1R} attains its maximum value, i.e. the most amplified mode. This wavelength, which we will term λ_{max} is likely to be the wavelength of the early bedforms observed under these flow and bed conditions. In fact, we find the values of λ_{max} for the cases in Figure 5 and those observed in Zgheib et al. (2018a) to be in good agreement

19

with one another as shown in Table 4. Table 4 shows the preferred spacing of bedforms from the

temporally and spatially evolving coupled bed-flow simulations against the most amplified

wavelength from the present linear stability analysis. The first two rows in the table correspond

to the plots in Figure 5. The simulation parameters from Zgheib et al. (2018a) in the first row of

Table 4 in fact encompass multiple cases. All these cases have the same Froude and particle

Reynolds numbers, however the size, number, and placement of the sediment pileups at the start

of the simulation varied. By direct comparison between the first and third rows in Table 4, we

find the effect of Re_p on λ_{max} to be minor as the value of λ_{max} remains unchanged in both the

simulations of Zgheib et al. (2018a) and the present analysis. Needless to say that this is only

pertinent to the parametric set of those two simulations. Nonetheless, as we will show in Section

3.3, the effect of Re_p on λ_{max} appears to be marginal for a wide range of parameters.

We should note here that the agreement between the present stability analysis and Zgheib et al.

(2018a) does not constitute a full validation since the fixed bed simulations used in the stability

analysis are a truncation of the mobile bed simulations in Zgheib et al. (2018a).

3.3   *Sweeping the parameter space*

The plots in Figure 5 and the corresponding data in Table 4 are valid for a specific set of flow and

particle parameters, namely those used in the simulations of Zgheib et al. (2018a). In the case of

the DNS of an evolving bed, new simulations are required in order to investigate different flow

and particle parameters, or implement a different model for sediment transport. With the

present approach of linear stability analysis, provided Re_τ remains unchanged, no new

simulations are required to sweep the particle parameters or to test different sediment transport

models. This is because in this linear stability analysis, once the bed shear stress is known, the stability analysis can be carried out for a wide set of physical or modelling parameters.

The bed shear stress constitutes the only simulation output needed in the analysis, which in turn represents the input to the Exner equation. The key bed shear stress results from the frozen sinusoidal bed simulations are shown in Figure 6 and tabulated in Table 5. Panel (a) shows the plane (streamwise and spanwise) and time averaged bed-normal gradient of tangential velocity, whereas panels (b) and (c) show the ratio of the first order bed-normal gradient of tangential velocity to the amplitude of bed height perturbation for the in-phase and out-of-phase components, respectively. These components are obtained through a Fourier decomposition as indicated in (8), namely

$$\partial \langle \bar{u}_t \rangle / \partial n = \partial \langle \bar{\bar{u}}_t \rangle / \partial n + (\partial \langle \bar{u}_t \rangle / \partial n)_1 e^{\alpha_1 t} e^{i\frac{2\pi x}{\lambda}} + complex\ conjugate + HOT\ . \qquad (11)$$

The three terms plotted in Figure 6 represent the simulation output that is sufficient to carry out the linear stability analysis. The mean component in panel (a) produces the $\langle \bar{\bar{\Theta}} \rangle$ term, which appears in both expressions for the growth rate and phase speed in (10). On the other hand, the in-phase and out-of-phase components determine the phase speed ($\langle \bar{\Theta} \rangle_{1R}$) and the growth rate ($\langle \bar{\Theta} \rangle_{1I}$), respectively.

For the fixed value of $Re_\tau = 180$, the simulation output of a specific mode (i.e. for a fixed value of λ) in terms of the bed shear stress, becomes only a function of the bed perturbation amplitude δ. Here the value of δ must be chosen small enough to obtain a linear response in the shear stress to the wavy bottom (Charru et al. 2013). Charru et al. (2013) argued that the response is linear when the ratio $2\delta/\lambda < 0.03$. For all the simulations in the present study, this condition was

satisfied and the ratio varied between $3.3 \times 10^{-4} \leq 2\delta/\lambda \leq 5.3 \times 10^{-3}$. Additionally, from Figure 6a, we find $\partial\langle\bar{\bar{u}}_t\rangle/\partial n$ to vary by less than 3% as λ decreases from 1 to 1/16. This indicates that the effects of the pressure drop due to the increased number of waves are minimal and the effective shear Reynolds number for all the simulations in Table 1 is nearly identical. To facilitate the use of the DNS data presented in Figure 6 for future modellers, we use a saturation growth curve fit for the data in panel (a), and a power law fit for the data in panels (b) and (c). The equations for each fit along with the coefficients are shown below.

$$\text{Saturation fit:} \quad \partial\langle\bar{\bar{u}}_t\rangle/\partial n = 175.7\frac{\lambda}{\lambda + 0.02309}$$

$$\text{Power law fit:} \quad \frac{(\partial\langle\bar{u}_t\rangle/\partial n)_{1R}}{h_{1R}} = 3888\lambda^{-1.245} \qquad (12)$$

$$\text{Power law fit:} \quad \frac{(\partial\langle\bar{u}_t\rangle/\partial n)_{1I}}{h_{1R}} = 2200\lambda^{-0.4748}$$

3.3.1 *Physical parameters*

The parameters that may potentially affect the maximum growth rate ($\alpha_{1R,max}$), wave speed of most amplified mode ($|\lambda_{max}\ \alpha_{1I,max}|$), and the wavelength of the most amplified mode (λ_{max}) may be split into two categories. The first category corresponds to physical parameters such as Re_τ, Re_p, Fr_τ, and χ. Here, Fr_τ and χ represent the Froude number and mean bed inclination, respectively (see Table 3). Whereas the second category consists of modelling parameters such as c_1, c_2, and ε. To investigate the effects of physical parameters, we considered a wide range of values for Re_p, Fr_τ, and χ. Recall, that all simulations had a fixed $Re_\tau = 180$. In Figure 7, we show the dependence of maximum growth rate, wavelength and wave speed of most amplified mode on the physical parameters. In all panels, we fix two of the physical parameters and allow the

third to vary to isolate its effect on incipient bed formation. As for the modelling parameters, c_1 and c_2 correspond to the Wong & Parker (2006) modified MPM model and $\varepsilon = 4$ was used as the diffusion coefficient (Cayocca 2001, Zgheib et al. 2018a,b). Unless otherwise stated, these aforementioned values will constitute the default values of the modelling parameters and will be used throughout the study.

In panels (a) to (c), we observe $\alpha_{1R,max}$, $|\lambda_{max}\,\alpha_{1I,max}|$, and λ_{max} to increase with Fr_τ. However, as can be seen from the figure, the rate of increase depends on Fr_τ. Since Re_τ is held fixed, then from panels (a) and (b) we find that for the same flow rate per unit width, the shallower the flow the quicker the emergence of bedforms and the faster the speed of these incipient bedforms. Additionally, the shallower the flow the larger the separation distance between incipient bedforms.

The variation in panels (d) and (e) is non-monotonic, unlike in panel (f) where λ_{max} continuously decreases with Re_p, consistent with the findings of Charru et al. (2013). . In fact, for the range of values considered for Fr_τ ($0.02 \leq Fr_\tau \leq 0.19$) and χ ($-25° \leq \chi \leq 25°$) we find a monotonic decrease in λ_{max} over an Re_p range of $1 \leq Re_p \leq 150$. On the other hand, if $Fr_\tau > 0.1$ and $\chi \leq 0$ (flat or downslope), then the decrease in wave speed ($|\lambda_{max}\,\alpha_{1I,max}|$) becomes monotonic over the entire Re_p range considered. However, for steep upslope currents, larger values of Fr_τ would be required to maintain a monotonic decrease in $\lambda_{max}\,\alpha_{1I,max}$ for the considered range of Re_p. The growth rate on the other hand remains non-monotonic and attains a minimum value for all Fr_τ and χ values considered. The value of Re_p at which this minimum occurs depends on

Fr_τ and χ. The larger the Froude number, or the smaller χ is, the larger the value of Re_p at which the minimum occurs.

Finally, in panels (g) to (i), we observe a monotonic dependence. This monotonic behaviour is also observed for all considered values of Re_p and Fr_τ. For increasing values of χ, we find the growth rate and wave speed to increase, while the spacing between incipient bedforms decreases.

By generating a multitude of plots with a wide range of parameters, we find λ_{max} to be most sensitive to variations in Fr_τ when the latter is small, ie. $Fr_\tau \lesssim 0.06$ (Note here that as indicated in Table 3, the Froude number is based on the shear velocity and not the bulk velocity. If Fr_b denotes the latter, then $Fr_b/Fr_\tau \approx 15.6$). For example, an increase in Fr_τ from 0.02 to 0.06 results in approximately a 60% increase in λ_{max}. Whereas a two order of magnitude increase in Re_p from 1.5 to 150 is necessary to achieve the same magnitude of variation in λ_{max}. Changes in the mean channel slope appear to have the lowest impact on incipient bedform spacing. Similarly for incipient bedform speed and growth rates, the Froude number appears to be the dominant physical parameter followed by Re_p and χ.

In the case of ripples, it is well established that the spacing of bedforms at near equilibrium is strongly dependent on particle size and consequently on Re_p, with little dependence on the shear velocity, and consequently on Fr_τ (e.g. Yalin, 1977, Flemming 2000, Claudin & Andreotti 2006). However, the relationship between the wavelength of fully developed and incipient ripples is still an open issue (Fourriere et al. 2010). In our simulations, we observe Fr_τ to be the dominant parameter for the incipient wavelength and Re_p to play a secondary role. This observation, which

is derived from the linear stability analysis is consistent with the early time evolution of the erodible bed direct numerical simulations of Zgheib et al*.* ([2018a](#)). It is also consistent with the fact that the bed shear velocity is a key parameter affecting the phase shift between sediment flux and bed topology ([Engelund & Fredsoe 1982](#)). The phase shift being of paramount importance in the stability of the bed. It still remains to be fully explained how the incipient linear dependence change over time to the final nonlinear dependence of the near-equilibrium bedforms.

3.3.2 *Modelling parameters*

As discussed previously, the bed is fixed and the flow is fully resolved. However, since the stability analysis is performed on the Exner equation ([6](#)), the analysis entails modelling of microscale processes. The modelling aspects that we are considering here are twofold: (i) the fitting coefficients from the empirical modelling of the bedload flux in terms of the bed shear stress and (ii) the diffusion coefficient in the Exner equation ε. We adopt the Wong & Parker ([2006](#)) modified MPM ([Meyer-Peter & Müller 1948](#)) formulation to compute the bedload flux. This section tests the sensitivity of the formation of incipient bedforms on these modelling parameters, namely c_1, c_2, and ε. However, since the dependence on c_1 can be easily deduced from ([10](#)), we will only investigate the sensitivity of incipient bedforms on c_2 and ε. Similar to [Figure 7](#), [Figure 8](#) shows the dependence of $\alpha_{1R,max}$, $\left|\lambda_{max}\,\alpha_{1I,max}\right|$, and λ_{max} on c_2 and ε by varying each parameter separately over a prescribed range while holding the other fixed. Additionally, physical parameters also need to be specified. While the curves shown in [Figure 8](#) correspond to a specific set of parameters, the conclusions have been drawn from consideration of a wide range of

parameters. In panels (a) to (c), we investigate the dependence on the power exponent of the MPM bedload model (c_2). For the set of parameters considered, we observe, at relatively small values of c_2, enhanced growth rates and wave speeds with increasing c_2 values. The opposite is true for relatively large values of c_2. On the other hand, the variation in λ_{max} is monotonic, decreasing with increasing values of c_2.

The dependence of incipient bedforms on c_2 is strongly associated with other parameters such as Re_p and Fr_τ. Nonetheless, as in the case of physical parameters in , we observe monotonic variation in λ_{max} with c_2. For all cases considered, we find λ_{max} to decrease with increasing the MPM power coefficient c_2. The range over which λ_{max} varies as c_2 is modified increases for larger values of Fr_τ or smaller values of Re_p. That is to say, if in c the value of $Fr_\tau = 0.06$ is used instead of $Fr_\tau = 0.03$, then λ_{max} would have decreased from 4.3 to 1.5 (instead of from 2.7 to 1.3) when c_2 is increased from 1 to 2. This is also true for the growth rate and wave speed in panels (a) and (b). The range over which the growth rate or wave speed varies increases as larger Fr_τ or smaller Re_p values are considered. Nonetheless, because of the complex interaction of physical and modelling parameters in (10), it is difficult to setup regions for monotonic behaviour for $\alpha_{1R,max}$ or $|\lambda_{max} \, \alpha_{1I,max}|$.

As for the diffusion coefficient ε, its purpose is to dampen bedforms with very small wavelengths. As such, we observe λ_{max} in panel (f) to increase with increasing values of ε. Additionally, we observe in panels (d) and (e) a monotonic decrease in growth rate and wave speed with a stronger diffusion term. The response to ε is monotonic for all cases considered.

In Table 6 we show the trend for the growth rate, wave speed, and wavelength of the most amplified mode as a function of the physical and numerical parameters from Sections 3.3.1 and 3.3.2, respectively. We note the following

i.   The variation in λ_{max} is monotonic for all variables considered.
ii. The variation with respect to Fr_τ is monotonic. $\alpha_{1R,max}$, $\left|\lambda_{max}\,\alpha_{1I,max}\right|$, and λ_{max} increase with Fr_τ.
iii. The variation with respect to χ is monotonic. $\alpha_{1R,max}$ and $\left|\lambda_{max}\,\alpha_{1I,max}\right|$ increase with χ, while λ_{max} decreases with χ.
iv. The variation with respect to ε is monotonic. $\alpha_{1R,max}$ and $\left|\lambda_{max}\,\alpha_{1I,max}\right|$ decrease with ε, while λ_{max} increases with ε
v.   The variation with respect to Re_p and c_2 is non-monotonic and depends on a variety of factors.
vi. For cases in which the Fr_τ is held fixed, the larger the value of Fr_τ, the larger the range over which $\alpha_{1R,max}$, $\left|\lambda_{max}\,\alpha_{1I,max}\right|$, and λ_{max} vary.

4. Evolution of a Gaussian bedform wavepacket

In verifying Coleman & Melville's (1996) theory on bedform initiation, Zgheib et al. (2018a) conducted a series of simulations where a small two-dimensional Gaussian bump (Gaussian along both horizontal directions) was introduced to an otherwise flattened bed. The presence of the bump constituted a disturbance to the flow, which accelerated the formation of incipient bedforms. Zgheib et al. (2018a) observed that regardless of the size of the bump (provided it is of the order of a few particles), the bump straightened and progressively led to the formation of a train of incipient bedforms at a preferred spacing λ_p as shown in Figure 9. The setup for these "Gaussian bump" simulations is similar to the present setup except that the bed was allowed to evolve in response to the overlying turbulent flow.

Figure 9 shows a top view snapshot of the bed at $t_b = 47$ (see Table 3 for definition) with iso-contours of bed elevation η from the 2D Gaussian bump simulations of Zgheib et al. (2018a). The bed shows the presence of three incipient bedforms at a preferred spacing λ_p. The first bedform

on the left evolved from the initial 2D Gaussian bump, whose initial x-y location is marked on the figure by a solid black circle. The subsequent bedforms progressively formed after the Gaussian bump flattens, becoming locally two-dimensional. To provide a quantitative value of λ_p, we performed a two-dimensional Fourier decomposition of η at the instance shown in the figure. The amplitude (A) of the two largest amplified streamwise modes are highlighted in the subset of Figure 9. All the streamwise modes were obtained for a zero spanwise mode, i.e. $k_y = 0$. We find $k_x = 8$ (highlighted in red) and $k_x = 10$ (highlighted in blue) to be the most significant modes. Recall that the streamwise length of the domain is $L_x = 12$, and thus the modes $k_x = 8$ and $k_x = 10$ signify a wavelength of 1.5 and 1.2, respectively. Thus, the result shown in Figure 8 is consistent with the quantitative result of $\lambda_p = 1.4$ in the figure.

Since the same preferred spacing λ_p was observed for various dimensions of the Gaussian bump (Zgheib et al. 2018a), one may argue that this preferred separation λ_p is independent of the bump, which led to the formation of this train of incipient bedforms. If this is the case, then the separation distance λ_p must be tied to some other inherent length scale, in the flow or with the particle parameters. This idea is further supported by the fact that for an initially perfectly flattened bed, incipient bedforms formed at the same preferred spacing λ_p. The emergence of the incipient bedforms was however delayed in comparison to the case where a Gaussian bump was initially present. Thus, the presence of the Gaussian bump acted as a catalyst to speed the evolution of the bed.

Because of the nearly two-dimensional nature of the train of incipient bedforms in Figure 9, we carried out an additional simulation that corresponds to the one-dimensional version of the

Gaussian bump simulation in Zgheib et al. (2018a). Instead of a 2D Gaussian bump that varied along both horizontal directions, we use a one-dimensional Gaussian ridge with the same amplitude and width as the bump, but that extends across the entire width of the channel. The bed height elevation at the start of the simulation may be expressed by the following Gaussian profile

$$\eta = A_R exp\left[-\frac{(x - x_0)^2}{2\delta_B^2}\right],\qquad(13)$$

where $A_R = 0.02$ and $\delta_B = 0.1$ represent the amplitude and width of the ridge, respectively. There values are identical to those used in the Gaussian bump simulation shown in Figure 9. This simulation is different from those described in Section 3. Here, the bed is allowed to evolve in response to the bed shear stress according to (3). However, the start of the simulation occurs once the flow has reached a stationary state. That is, the bed remains fixed until the turbulent flow becomes fully developed, and only then is the bed allowed to evolve. As seen in Figure 10, the effect of the ridge is different from the bump in terms of the spacing or preferred wavelength of the newly formed incipient bedform. Figure 10 shows a top view at $t_b = 0$ (panel (a)) and $t_b = 47$ (panel (b)). The bed at the start of the simulation is completely flat except for the presence of the Gaussian ridge. After the bed is allowed evolve, we observe the new incipient bedform to form at a distance of 1.9 flow depths, which is more than 30% larger than the preferred spacing observed for the Gaussian bump simulations in Figure 9.

In the case of the three-dimensional bump, the flow is allowed to negotiate its path over and around the bump. On the other hand, for the two-dimensional ridge, the flow may only go over the ridge. This results in a longer wake downstream of the ridge, which in turn causes a larger

downstream distance affected by the ridge. This is despite the fact that both the ridge and bump have the same amplitude and width and share the same flow and particle properties. However, the larger spacing between the original ridge and the newly formed bump could also be affected by other factors such as the initial amplitude and width of the Gaussian ridge.

One may argue that the isolated bump is more relevant, as compared to the Gaussian ridge, to the early time evolution of bedforms from an initially flat bed. This is because the near bed turbulent flow field is inherently three-dimensional, and as such the initial perturbation to the underlying flat bed is correspondingly three-dimensional.

We should note here that in the present simulations, only the meso scale turbulence is resolved, while the microscale flow around the individual sediments (or pseudo turbulence) is not resolved. In this approach the carrier phase governing equations have been implicitly averaged on a scale an order of magnitude large than the sediment diameter and the DNS is of this implicitly averaged flow. As a result the bed has been resolved only at the meso-scale, i.e, on a scale an order of magnitude (or more) larger than the individual sediment.

Thus, in the present simulations, each Eulerian grid cell on the bed contains a large number of sediment, whose collective motion dictates the evolution of the bed at the meso-scale. The simulations are therefore only resolved at the mesoscale for both the flow as well as the sediment – i.e, both the flow and sediment motion are resolved only on scales much larger than a sediment diameter. It is in this sense of meso-scale collective motion of sediment we use the MPM modified Wong & Parker (2006) formulation.

5. Conclusions

We presented results from linear stability analysis on the incipient motion of ripples in a turbulent, open-channel unidirectional flow. The analysis was coupled with direct numerical simulations of flow over both fixed, and erodible, sediment bed. The immersed boundary method was used to account for the presence of the bed by forcing the no-slip and no-penetration conditions at the bed-fluid interface. A total of 11 fixed-bed simulations were carried out at the same shear Reynolds number of 180. In each of these simulations, the sediment bed (i.e. the immersed boundary) was sinusoidally perturbed along the streamwise direction (i.e. with no spanwise variation) with different wavelengths. We should note here that while the bed topology is two-dimensional and therefore does not admit any spanwise variation, the simulations are fully three-dimensional.

Linear stability analysis was performed using the Exner equation with input extracted from the simulations in the form of sediment flux. To that end, after the simulations run long enough to reach stationary conditions, the bed shear stress from each simulation was span and time averaged. The sediment flux is then computed from this averaged shear stress using the MPM formulation. One of the main advantages of this approach is that the phase shift between the sediment flux and the bed topology comes out naturally from the simulations.

The main purpose of the paper was to assess the dependence of the incipient bedforms on a variety of parameters. To that end, we performed a parametric study where we varied multiple physical and modelling parameters. In the case of physical parameters, we varied the Froude and particle Reynolds number as well as the mean bed slope. As for the modelling parameters, we varied the coefficients in the MPM formulation as well as the diffusion coefficient in the Exner

equation. We found the most unstable mode, λ_{max}, to vary monotonically with all considered parameters. More specifically, we found λ_{max} to increase with Froude number and decrease with mean channel slope and particle Reynolds number.

We found the Froude number to be the controlling parameter for initial bedform development while the role of all the other parameters considered was found to be less critical when compared to the Froude number. This is in contrast with the dominant role of the particle Reynolds number during the equilibrium stage of bedforms, at least in the case of ripples. Moreover, for the cases in which the Froude number is held fixed, the larger its value, the larger the range over which the dominant wavelength, growth rate and phase speed of incipient bedforms varied. The results from the linear stability analysis were in good agreement with previously published data on time evolving, coupled, bed-flow direct numerical simulations (Zgheib et al. 2018 a, b).

In addition to the fixed-bed simulations, a wave packet analysis was also conducted. Here a small amplitude, one-dimensional Gaussian ridge was allowed to evolve under a stationary turbulent flow. The analysis on the wave packet revealed a larger incipient wavelength than that produced by the two-dimensional Gaussian bump with identical height and width. This was attributed to the fact that in the case of the two-dimensional bump, the flow is allowed to negotiate its path over and around the bump. On the other hand, for the one-dimensional ridge, the flow may only go over the ridge, which results in a larger downstream distance affected by the ridge.

REFERENCES

Akiki, G., & Balachandar, S. (2016). Immersed boundary method with non-uniform distribution of Lagrangian markers for a non-uniform Eulerian mesh. *Journal of Computational Physics*, *307*, 34-59.

Ancey, C. (2010). Stochastic modeling in sediment dynamics: Exner equation for planar bed incipient bed load transport conditions. *Journal of Geophysical Research: Earth Surface*, *115*(F2).

Andreotti, B., Claudin, P., & Pouliquen, O. (2006). Aeolian sand ripples: experimental study of fully developed states. *Physical review letters*, *96*(2), 028001.

Apte, S. V., Mahesh, K., & Lundgren, T. (2008). Accounting for finite-size effects in simulations of disperse particle-laden flows. *International Journal of Multiphase Flow*, *34*(3), 260-271.

Baas, J. H. (1994). A flume study on the development and equilibrium morphology of current ripples in very fine sand. *Sedimentology*, *41*(2), 185-209.

Baas, J. H. (1999). An empirical model for the development and equilibrium morphology of current ripples in fine sand. *Sedimentology*, *46*(1), 123-138.

Bennett, S. J., & Best, J. L. (1995). Mean flow and turbulence structure over fixed, two-dimensional dunes: implications for sediment transport and bedform stability. *Sedimentology*, *42*(3), 491-513.

Blondeaux, P. (1990). Sand ripples under sea waves Part 1. Ripple formation. *Journal of Fluid Mechanics*, *218*, 1-17.

Bohorquez, P., & Ancey, C. (2015). Stochastic-deterministic modeling of bed load transport in shallow water flow over erodible slope: Linear stability analysis and numerical simulation. *Advances in water resources*, *83*, 36-54.

Bridge, J. S., & Best, J. L. (1988). Flow, sediment transport and bedform dynamics over the transition from dunes to upper-stage plane beds: implications for the formation of planar laminae. *Sedimentology*, *35*(5), 753-763.

Calhoun, R. J., & Street, R. L. (2001). Turbulent flow over a wavy surface: Neutral case. *Journal of Geophysical Research: Oceans*, *106*(C5), 9277-9293.

Camporeale, C., & Ridolfi, L. (2011). Modal versus nonmodal linear stability analysis of river dunes. *Physics of Fluids*, *23*(10), 104102

Cantero, M. I., Balachandar, S., & Garcia, M. H. (2007). High-resolution simulations of cylindrical density currents. *Journal of Fluid Mechanics*, *590*, 437-469.

Caruso, A., Vesipa, R., Camporeale, C., Ridolfi, L., & Schmid, P. J. (2016). River bedform inception by flow unsteadiness: A modal and nonmodal analysis. *Physical Review E*, *93*(5), 053110.

Cayocca, F. (2001). Long-term morphological modeling of a tidal inlet: the Arcachon Basin, France. *Coastal Engineering*, *42*(2), 115-142.

Chakraborty, P., Balachandar, S., & Adrian, R. J. (2005). On the relationships between local vortex identification schemes. Journal of Fluid Mechanics, 535, 189–214. https://doi.org/10.1017/S0022112005004726

Charru, F., Andreotti, B., & Claudin, P. (2013). Sand ripples and dunes. *Annual Review of Fluid Mechanics*, *45*, 469-493.

Charru, F., & Mouilleron-Arnould, H. (2002). Instability of a bed of particles sheared by a viscous flow. *Journal of Fluid Mechanics*, *452*, 303-323.

Cherukat, P., Na, Y., Hanratty, T. J., & McLaughlin, J. B. (1998). Direct numerical simulation of a fully developed turbulent flow over a wavy wall. *Theoretical and computational fluid dynamics*, *11*(2), 109-134.

Chiew, Y. M., & Parker, G. (1994). Incipient sediment motion on non-horizontal slopes. *Journal of Hydraulic Research*, *32*(5), 649-660.

Chou, Y. J., & Fringer, O. B. (2010). A model for the simulation of coupled flow-bed form evolution in turbulent flows. *Journal of Geophysical Research: Oceans*, *115*(C10).

Claudin, P., & Andreotti, B. (2006). A scaling law for aeolian dunes on Mars, Venus, Earth, and for subaqueous ripples. Earth and Planetary Science Letters, 252(1-2), 30–44. https://doi.org/10.1016/j.epsl.2006.09.004

Coleman, S. E., & Eling, B. (2000). Sand wavelets in laminar open-channel flows. *Journal of Hydraulic Research*, *38*(5), 331-338.

Coleman, S. E., & Melville, B. W. (1994). Bed-form development. *Journal of hydraulic engineering*, *120*(5), 544-560.

Coleman, S. E., & Melville, B. W. (1996). Initiation of bed forms on a flat sand bed. *Journal of Hydraulic Engineering*, *122*(6), 301-310.

Colombini, M. (2004). Revisiting the linear theory of sand dune formation. *Journal of Fluid Mechanics*, *502*, 1-16.

Colombini, M., & Stocchino, A. (2011). Ripple and dune formation in rivers. *Journal of Fluid Mechanics*, *673*, 121-131.

Cortese, T. A., & Balachandar, S. (1995). High performance spectral simulation of turbulent flows in massively parallel machines with distributed memory. *International Journal of High Performance Computing Applications*, *9*(3), 187-204.

Engelund, F. (1970). Instability of erodible beds. *Journal of Fluid Mechanics*, *42*(02), 225-244.

Engelund, F., & Fredsoe, J. (1982). Sediment ripples and dunes. *Annual Review of Fluid Mechanics*, *14*(1), 13-37.

Escauriaza, C., & Sotiropoulos, F. (2011). Initial stages of erosion and bed form development in a turbulent flow around a cylindrical pier. *Journal of Geophysical Research: Earth Surface*, *116*(F3).

Flemming, B. W. (2000). The role of grain size, water depth and flow velocity as scaling factors controlling the size of subaqueous dunes. In Marine sandwave dynamics, International Workshop (pp. 23–24). Lille, France

Fourriere, A., Claudin, P., & Andreotti, B. (2010). Bedforms in a turbulent stream: formation of ripples by primary linear instability and of dunes by nonlinear pattern coarsening. *Journal of Fluid Mechanics*, *649*, 287-328.

Hudson, J. D., Dykhno, L., & Hanratty, T. J. (1996). Turbulence production in flow over a wavy wall. *Experiments in Fluids*, *20*(4), 257-265.

Khosronejad, A., Kang, S., Borazjani, I., & Sotiropoulos, F. (2011). Curvilinear immersed boundary method for simulating coupled flow and bed morphodynamic interactions due to sediment transport phenomena. *Advances in water resources*, *34*(7), 829-843.

Kennedy, J. F. (1969). The formation of sediment ripples, dunes, and antidunes. *Annual Review of Fluid Mechanics*, *1*(1), 147-168.

Kidanemariam, A. G., & Uhlmann, M. (2014). Direct numerical simulation of pattern formation in subaqueous sediment. *Journal of Fluid Mechanics*, *750*, R2.

Kidanemariam, A. G., & Uhlmann, M. (2017). Formation of sediment patterns in channel flow: minimal unstable systems and their temporal evolution. *Journal of Fluid Mechanics*, (accepted arXiv:1702.06648)

Kim, J., Moin, P., & Moser, R. (1987). Turbulence statistics in fully developed channel flow at low Reynolds number. *Journal of fluid mechanics*, *177*, 133-166.

Langlois, V., & Valance, A. (2007). Initiation and evolution of current ripples on a flat sand bed under turbulent water flow. *The European Physical Journal E*, *22*(3), 201-208.

Meyer-Peter, E., & Müller, R. (1948). Formulas for bed-load transport. In *IAHSR 2nd meeting, Stockholm, appendix 2*. IAHR.

McLean, S. R. (1990). The stability of ripples and dunes. *Earth-Science Reviews*, *29*(1-4), 131-144.

Nabi, M., Vriend, H. J., Mosselman, E., Sloff, C. J., & Shimizu, Y. (2013). Detailed simulation of morphodynamics: 3. Ripples and dunes. Water Resources Research, 49, 5930–5943. https://doi.org/10.1002/wrcr.20457

Nakagawa, H., & Tsujimoto, T. (1984). Spectral analysis of sand bed instability. *Journal of Hydraulic Engineering*, *110*(4), 467-483.

Ouriemi, M., Aussillous, P., & Guazzelli, E. (2009a). Sediment dynamics. Part 1. Bed-load transport by laminar shearing flows. *Journal of Fluid Mechanics*, *636*, 295-319.

Ouriemi, M., Aussillous, P., & Guazzelli, E. (2009b). Sediment dynamics. Part 2. Dune formation in pipe flow. *Journal of Fluid Mechanics*, *636*, 321-336.

Paola, C., & Voller, V. R. (2005). A generalized Exner equation for sediment mass balance. *Journal of Geophysical Research: Earth Surface*, *110*(F4).

Paarlberg, A. J., Dohmen-Janssen, C. M., Hulscher, S. J., & Termes, P. (2009). Modeling river dune evolution using a parameterization of flow separation. *Journal of Geophysical Research*, 114, F01014. https://doi.org/10.1029/2007JF000910

Perillo, M. M., Prokocki, E. W., Best, J. L., & Garcia, M. H. (2014). Bed form genesis from bed defects under unidirectional, oscillatory, and combined flows. *Journal of Geophysical Research: Earth Surface*, *119*(12), 2635-2652.

Rauen, W. B., Binliang, L. I. N., & Falconer, R. A. (2008). Transition from wavelets to ripples in a laboratory flume with a diverging channel. *International Journal of Sediment Research*, *23*(1), 1-12.

Richards, K. J. (1980). The formation of ripples and dunes on an erodible bed. *J. Fluid Mech*, *99*(3), 597-618.

Robert, A., & Uhlman, W. (2001). An experimental study on the ripple–dune transition. *Earth Surface Processes and Landforms*, *26*(6), 615-629.

Shields, A. (1936). Application of similarity principles and turbulence research to bed-load movement. Soil Conservation Service.

Shringarpure, M., Cantero, M. I., & Balachandar, S. (2012). Dynamics of complete turbulence suppression in turbidity currents driven by monodisperse suspensions of sediment. *Journal of Fluid Mechanics*, *712*, 384-417.

Sotiropoulos, F., & Khosronejad, A. (2016). Sand waves in environmental flows: Insights gained by coupling large-eddy simulation with morphodynamics. *Physics of Fluids*, *28*(2), 021301.

Sun, R., & Xiao, H. (2016). CFD–DEM simulations of current-induced dune formation and morphological evolution. *Advances in water resources*, *92*, 228-239.

Uhlmann, M. (2005). An immersed boundary method with direct forcing for the simulation of particulate flows. *Journal of Computational Physics*, *209*(2), 448-476.

Venditti, J. G., Church, M. A., & Bennett, S. J. (2005). Bed form initiation from a flat sand bed. *Journal of Geophysical Research: Earth Surface*, *110*(F1).

Vesipa, R., Camporeale, C., & Ridolfi, L. (2012). A shallow-water theory of river bedforms in supercritical conditions. *Physics of Fluids*, *24*(9), 094104.

Wong, M., & Parker, G. (2006). Reanalysis and correction of bed-load relation of Meyer-Peter and Müller using their own database. *Journal of Hydraulic Engineering*, *132*(11), 1159-1168.

Yalin, M. S. (1977). Mechanics of sediment transport. Tarrytown, New York: Pergamon.

Zgheib, N., Fedele, J. J., Hoyal, D. C. J. D., Perillo, M. M., & Balachandar, S. (2018a). Direct numerical simulation of transverse ripples: 1. Pattern initiation and bedform interactions. *Journal of Geophysical Research: Earth Surface*.

Zgheib, N., Fedele, J. J., Hoyal, D. C. J. D., Perillo, M. M., & Balachandar, S. (2018b). Direct Numerical Simulation of Transverse Ripples: 2. Self-Similarity, Bedform Coarsening, and Effect of Neighboring Structures. *Journal of Geophysical Research: Earth Surface*.

Zhou, J., Adrian, R. J., Balachandar, S., & Kendall, T. M. (1999). Mechanisms for generating coherent packets of hairpin vortices in channel flow. *Journal of Fluid Mechanics*, 387, 353–396. https://doi.org/10.1017/S002211209900467X

Zilker, D. P., Cook, G. W., & Hanratty, T. J. (1977). Influence of the amplitude of a solid wavy wall on a turbulent flow. Part 1. Non-separated flows. *Journal of Fluid Mechanics*, *82*(1), 29-51.

Tables & Figures

Table 1. List of fixed bed simulations with streamwise sinusoidal perturbation. λ and δ are the wavelength and amplitude of the sinusoidal disturbance of the bed.

Simulation number	Re_τ	λ	δ	$L_x \times L_y \times L_z$	$N_x \times N_y \times N_z$
S0	180	∞	0	$12 \times 4 \times 1.005$	$288 \times 96 \times 301$
S1	180	$L_x/1$	2×10^{-3}	$12 \times 4 \times 1.005$	$288 \times 96 \times 301$
S2	180	$L_x/2$	2×10^{-3}	$12 \times 4 \times 1.005$	$288 \times 96 \times 301$
S3	180	$L_x/3$	2×10^{-3}	$12 \times 4 \times 1.005$	$288 \times 96 \times 301$
S4	180	$L_x/4$	2×10^{-3}	$12 \times 4 \times 1.005$	$288 \times 96 \times 301$
S6	180	$L_x/6$	2×10^{-3}	$12 \times 4 \times 1.005$	$288 \times 96 \times 301$
S8	180	$L_x/8$	2×10^{-3}	$12 \times 4 \times 1.005$	$288 \times 96 \times 301$
S10	180	$L_x/10$	2×10^{-3}	$12 \times 4 \times 1.005$	$288 \times 96 \times 301$
S12	180	$L_x/12$	2×10^{-3}	$12 \times 4 \times 1.005$	$288 \times 96 \times 301$
S14	180	$L_x/14$	2×10^{-3}	$12 \times 4 \times 1.005$	$288 \times 96 \times 301$
S16	180	$L_x/16$	2×10^{-3}	$12 \times 4 \times 1.005$	$288 \times 96 \times 301$

Table 2. Hydrodynamic and bedform deformation time scales.

	Hydrodynamic time scale	Bedform deformation time scale
Fast	$\dfrac{\text{Bulk velocity}}{\text{Grid spacing}}$	$\dfrac{\text{Shear velocity}}{\text{Grain Diameter}}$
Slow	$\dfrac{\text{Bulk velocity}}{\text{Domain height}}$	$\dfrac{\text{Shear velocity}}{\text{Bedform wavelength}}$

Table 3. Symbols, notation, and nomenclature definition. (* denotes dimensional quantity).

Variable/Notation	Symbol	Mathematical expression
Mean flow depth (length scale)	H_f^*	-
Shear velocity (velocity scale)	U_τ^*	-
Time scale	Ψ^*	H_f^*/U_τ^*
3D velocity vector	$\boldsymbol{u}$	-
Unit vectors along the streamwise, spanwise, vertical, bed-tangent, and bed-normal directions	$\{\boldsymbol{e}_x, \boldsymbol{e}_y, \boldsymbol{e}_z, \boldsymbol{e}_t, \boldsymbol{e}_n\}$	-
Bulk velocity	U_b^*	$\dfrac{1}{L_y L_z}\displaystyle\int_0^{L_y}\int_0^{L_z} \boldsymbol{u}\cdot\boldsymbol{e}_x\, dzdy$
time	t^*	-
Bulk time	t_b	$t^* U_b^*/H_f^*$
Bed volume fraction	φ	-
Diffusion coefficient	ϵ	-
Bed elevation (w.r.t mean)	η	-
Particle diameter	d_p^*	-
Particle density	ρ_p^*	-
Fluid density	ρ_f^*	-
Submerged specific gravity	R	$(\rho_p^* - \rho_f^*)/\rho_f^*$
Gravitational acceleration	g^*	-
Fluid kinematic viscosity	ν^*	-
Fluid dynamic viscosity	μ^*	-
Particle Reynolds number	Re_p	$\dfrac{1}{\nu^*}\sqrt{R g^* d_p^{*3}}$
Shear Reynolds number	Re_τ	$U_\tau^* H_f^*/\nu^*$
Froude number	Fr_τ	$U_\tau^*/\sqrt{g^* H_f^*}$
Bed-normal velocity gradient	$\partial u/\partial n$	-
Bed shear stress	τ^*	$\left(\dfrac{\mu^* U_\tau^*}{H_f^*}\right)\dfrac{\partial u}{\partial n}$
Shields number	Θ	$\tau^*/[(\rho_p^* - \rho_f^*)g^* d_p^*]$
Critical Shields number on a flat bed ($\chi = 0$)	Θ_{cr0}	$\dfrac{1}{2}\left[0.22\, Re_p^{-0.6} + 0.06\, exp\left(-17.77\, Re_p^{-0.6}\right)\right]$
Critical Shields number on a non-flat bed ($\chi \neq 0$) (Chiew & Parker 1994)	Θ_{cr}	$\Theta_{cr} = \Theta_{cr0}\cos(\chi)\left[1 + \dfrac{\tan(\chi)}{\tan(\chi_r)}\right]$
Volumetric flux per unit width[א]	q	$q = (Re_p/Re_\tau)\, c_1(\Theta - \Theta_{cr})^{c_2}$
Volumetric flux with averaging	$\bar{q}, Q$	see (7)
Bed perturbation amplitude	δ	-
Bed perturbation wavelength	λ	-
Mean bed inclination	χ	-
Angle of repose	χ_r	$\chi_r = \pi/6$
Bed perturbation growth rate (complex quantity)	α_1	-
Numerical domain size (streamwise × spanwise × vertical)	$L_x \times L_y \times L_z$	-
Numerical resolution	$N_x \times N_y \times N_z$	-
Time average of quantity ■	$\langle\blacksquare\rangle$	$\dfrac{1}{T}\displaystyle\int_{t_1}^{t_1+T}\blacksquare\, dt$
Spanwise average of quantity ■	$\bar{\blacksquare}$	$\dfrac{1}{L_y}\displaystyle\int_0^{L_y}\blacksquare\, dy$
Stream and span average of quantity ■	$\bar{\bar{\blacksquare}}$	$\dfrac{1}{L_x L_y}\displaystyle\int_0^{L_y}\int_0^{L_x}\blacksquare\, dxdy$
n^{th} order of Fourier expansion of quantity ■	$\blacksquare_n$	-
Real and imaginary components of complex quantity ■	$\blacksquare_R$ & $\blacksquare_I$	-

[א] Based on MPM (1948) ($c_1 = 8, c_2 = 1.5$) and MPM modified Wong & Parker (2006) models ($c_1 = 4.93, c_2 = 1.6$)

Table 4. Most amplified wavelength from the temporally and spatially evolving simulations of Zgheib et al. (2018a) and the present linear stability analysis. The two bolded rows correspond to the cases in Figure 5.

Fr_τ	Re_p	λ_{max} (Zgheib et al. 2018a)	λ_{max} (stability analysis)
$\mathbf{3.27 \times 10^{-2}}$	$\mathbf{4.34}$	$\mathbf{\sim 1.4^{\aleph}}$	$\mathbf{\sim 1.5}$
$\mathbf{1.92 \times 10^{-2}}$	$\mathbf{4.34}$	$\mathbf{\sim 1.2}$	$\mathbf{\sim 0.93}$
3.27×10^{-2}	0.84	~ 1.4	~ 1.5

$^{\aleph}$ Same value of λ_{max} was observed for a variety of bump dimensions, and for different spacing of bumps when multiple bumps were present

Table 5. Tabulated data from Figure 6.

λ	$\partial\langle\bar{\bar{u}}_t\rangle/\partial n$	$(\partial\langle\bar{u}_t\rangle/\partial n)_{1R}/h_{1R}$	$(\partial\langle\bar{u}_t\rangle/\partial n)_{1I}/h_{1R}$
12	175	151	658
6	175	385	901
4	175	762	1156
3	174	1158	1351
2	174	1931	1668
1.5	173	2589	1893
1.2	173	3190	2061
1	172	3732	2212
0.857	171	4238	2293
0.75	170	4727	2348

Table 6. Trend in growth rate, wave speed, and wavelength of most amplified mode for physical and modelling parameters.

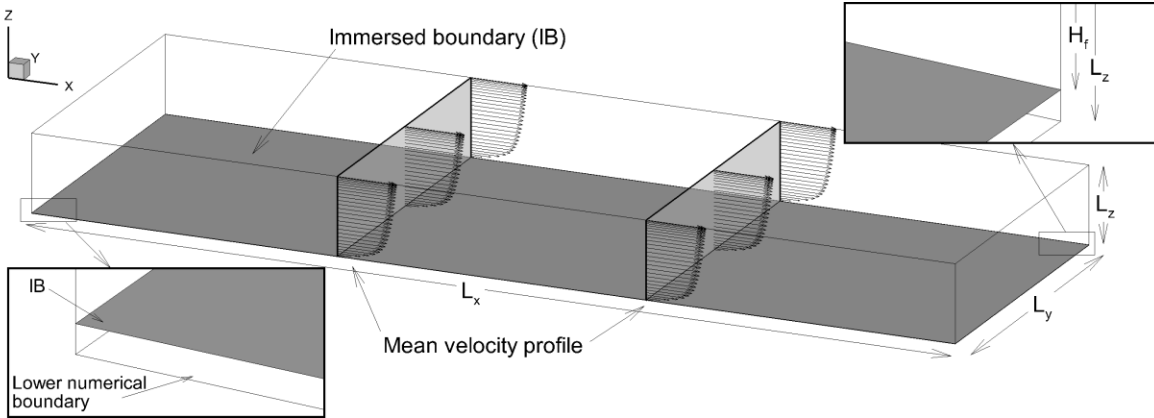|	Fr_τ ↗	Re_p ↗	χ ↗	c_1 ↗	ε ↗
λ_{max}	↗ monotonically	↘ monotonically	↘ monotonically	↘ monotonically	↗ monotonically
$\|\lambda_{max}\,\alpha_{1I,max}\|$	↗ monotonically	Depends on other parameters	↗ monotonically	Depends on other parameters	↘ monotonically
$\alpha_{1R,max}$	↗ monotonically	Depends on other parameters	↗ monotonically	Depends on other parameters	↘ monotonically

Figure 1. Numerical domain showing the time and plane-averaged velocity profile for the case of a fixed flat bed (S0). Periodic boundary conditions are enforced in the x and y directions. Free-slip and no-penetration are enforced at the top surface and no-slip/no-penetration conditions are enforced at the immersed boundary. The lower numerical domain shown in the bottom inset is rendered meaningless by the presence of the immersed boundary. The upper inset shows the lower extent of L_z and H_f. L_z corresponds to the distance between the top and bottom domain boundaries, whereas H_f which always has a non-dimensional value of unity represents the distance between the top domain boundary and the mean bed height elevation.
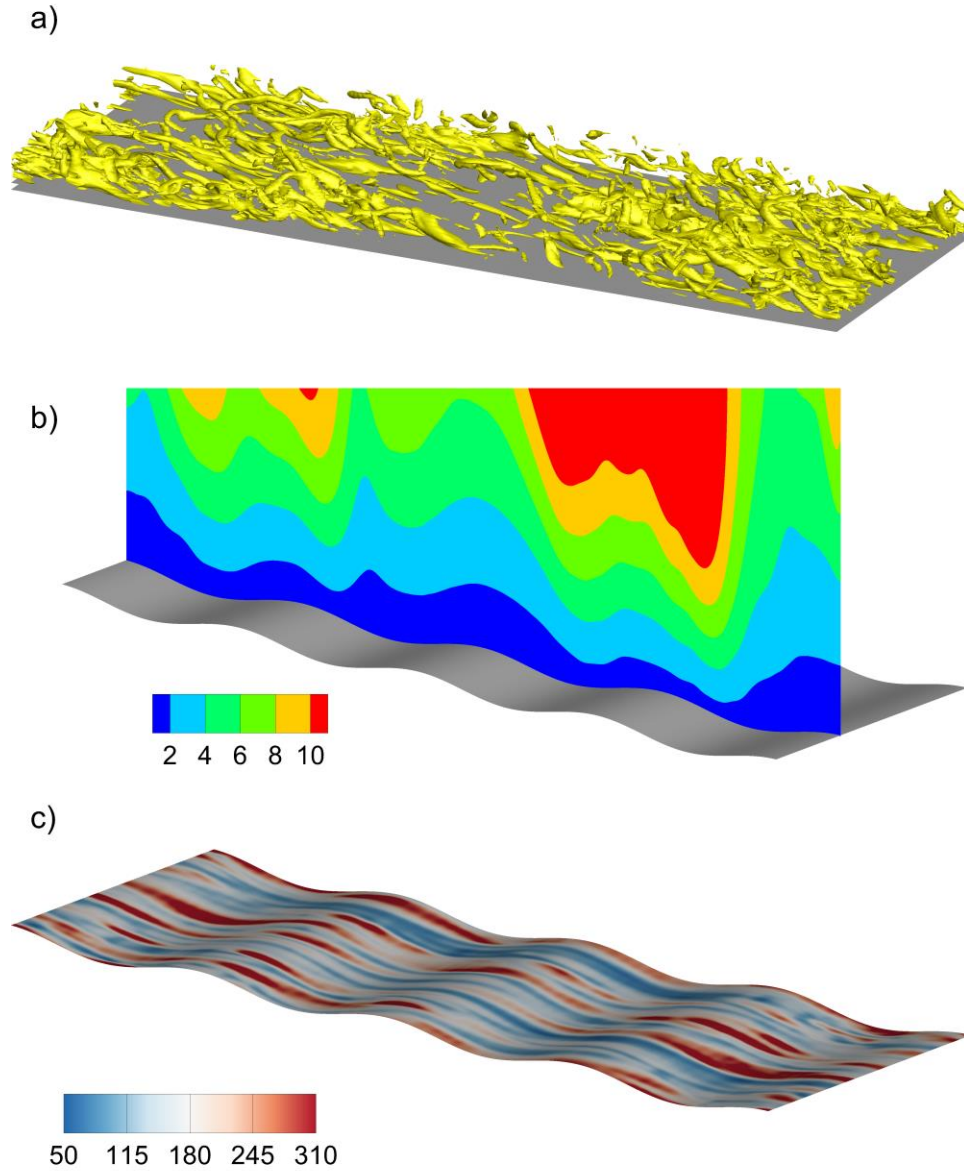
Figure 2. a) Iso-surfaces of the instantaneous swirling strength $\lambda_{ci} = 15$ (see text for definition) above the immersed boundary displaying hairpin and horseshoe vortices. b) Iso-contours of the instantaneous velocity in a vertical plane above the immersed boundary. c) Iso-contours of the instantaneous bed-normal gradient of tangential velocity $\partial u_t / \partial n$. In panels (b) and (c), the vertical z-direction is stretched by a factor of 50 to clearly show the sinusoidal shape of the bed. All figures correspond to the same instance of the fully developped turbulent flow from case S4.
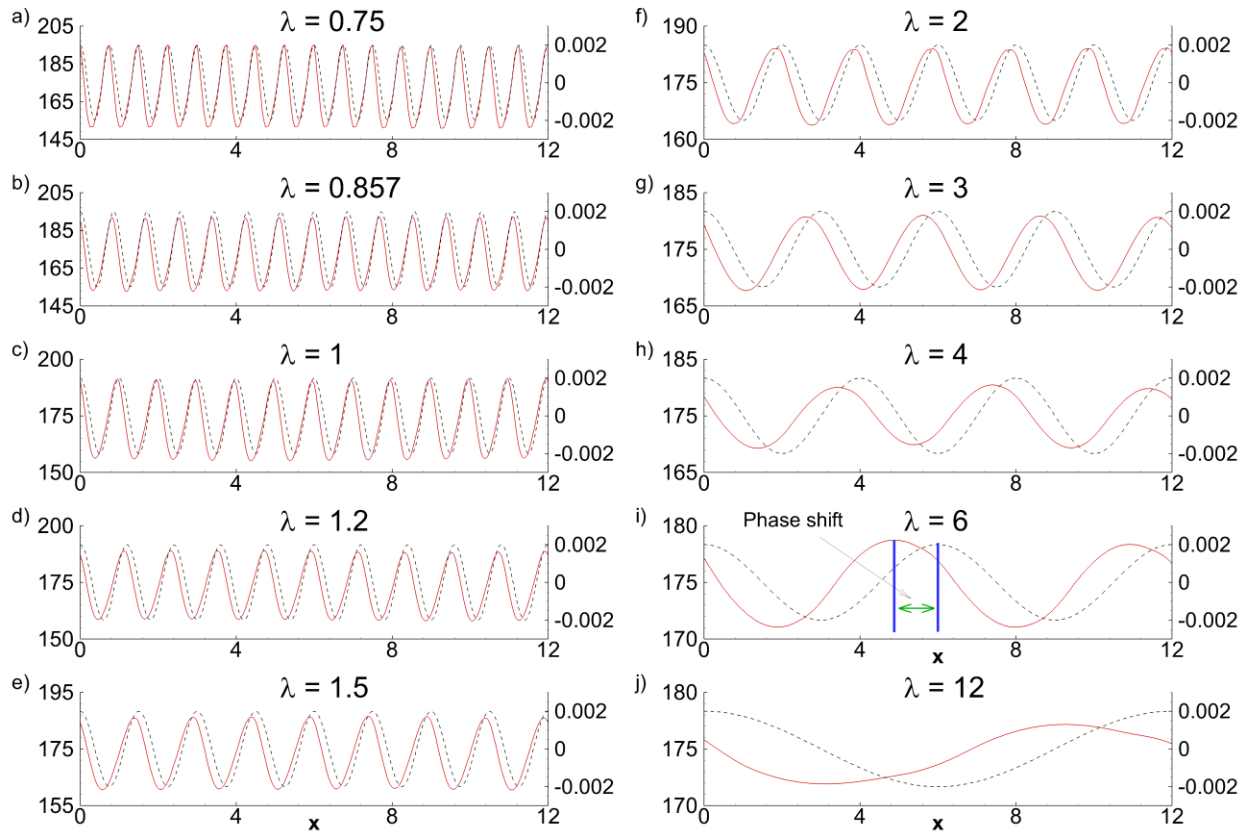
Figure 3. Streamwise variation of the span- and time-averaged bed normal gradient of tangential velocity $(\partial \langle \bar{u}_t \rangle / \partial n)$ (red solid line) for all cases in Table 1. The shape of the bed (black dashed line) is also included to indicate the phase shift between the two curves. The phase shift increases with the wavelength of the sinusoidal bed.
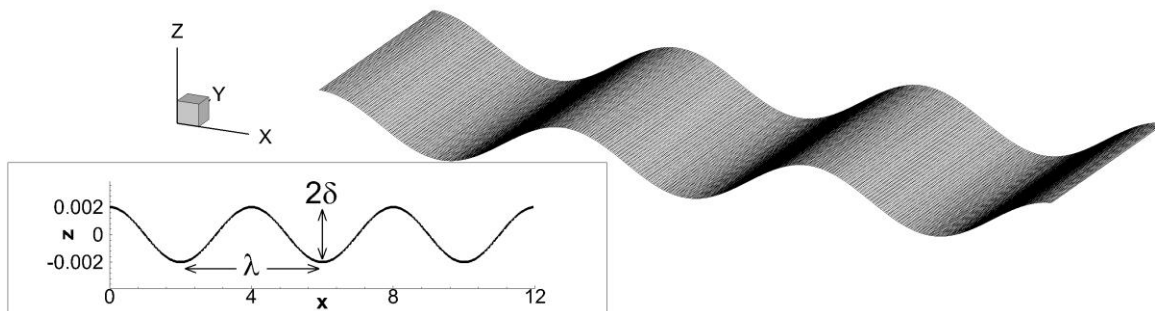
Figure 4. Shape of the bed (i.e. immersed boundary) for the two-dimensional linear stability analysis. The z-direction is stretched by a factor of 200 to illustrate the sinusoidal nature of the perturbation. The inset shows the true amplitude δ versus the wavelength λ of the perturbation.
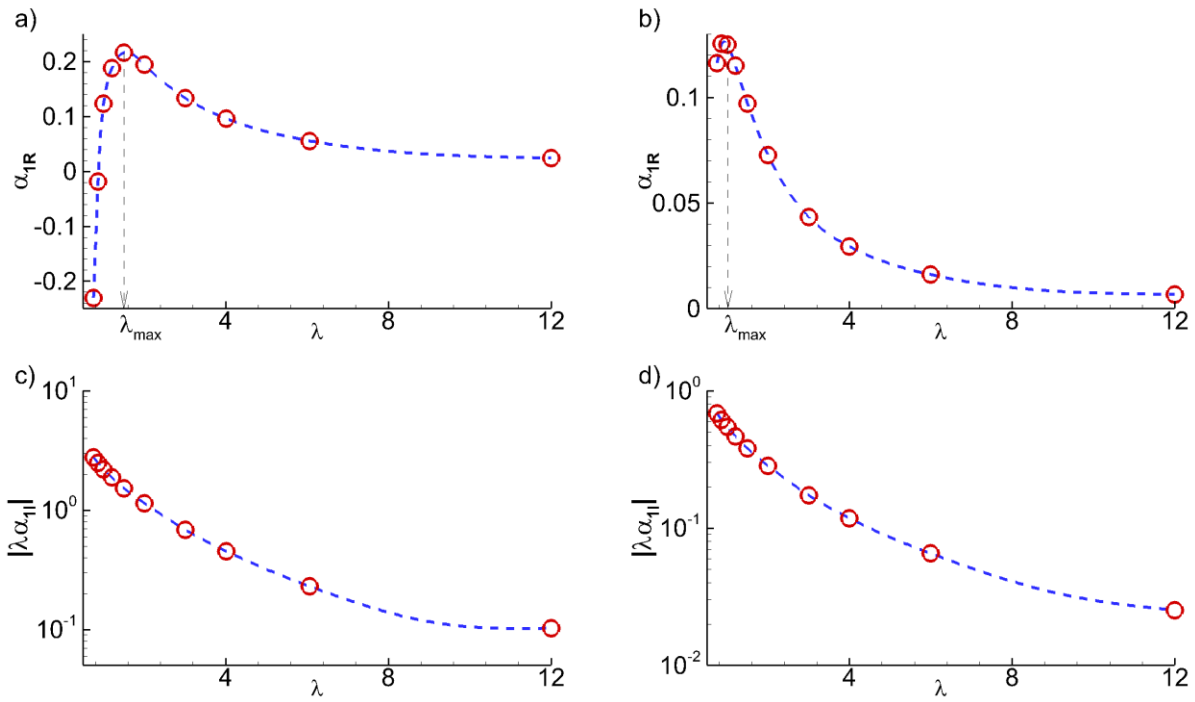
Figure 5. Growth rate α_{1R} versus wavelength λ obtained from the simulations in Table 1 for a) $Fr_\tau = 0.032$ & $Re_p = 4.34$ and c) $Fr_\tau = 0.019$ & $Re_p = 4.34$. b) and d) Same as a) and c) but for the aboslute value of the wave speed versus λ. The dashed line in a) and c) corresponds to the value of λ for which α_{1R} is a maximum.
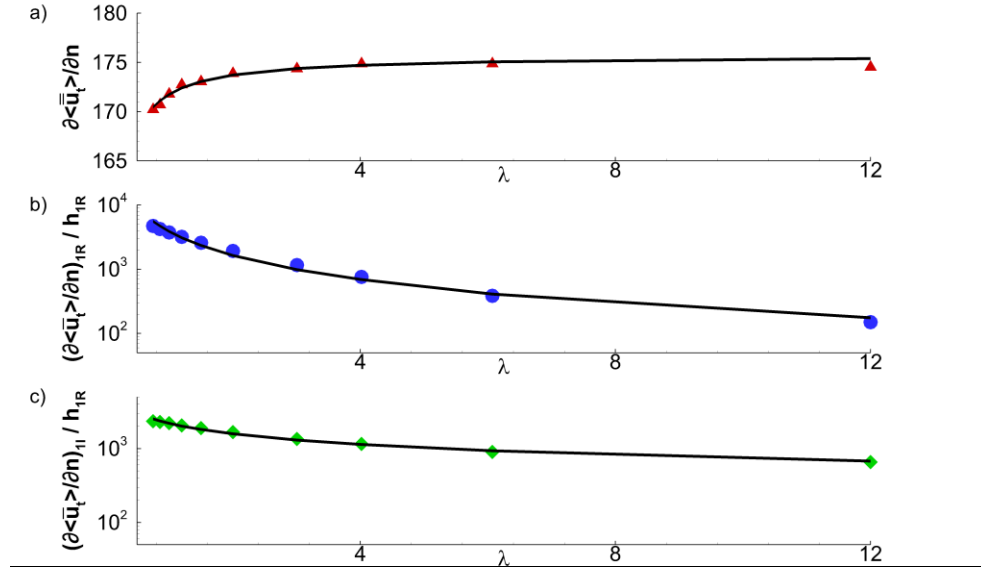
Figure 6. Direct numerical simulation output needed for linear stability analysis. a) Mean bed-normal gradient of tangential velocity. b) and c) Ratio of first order bed-normal gradient of tangential velocity to amplitude of bed height perturbation for the in-phase and out-of-phase components, respectively. The black solid curves in each panel correspond to the proposed fitting curves (see text for more details).
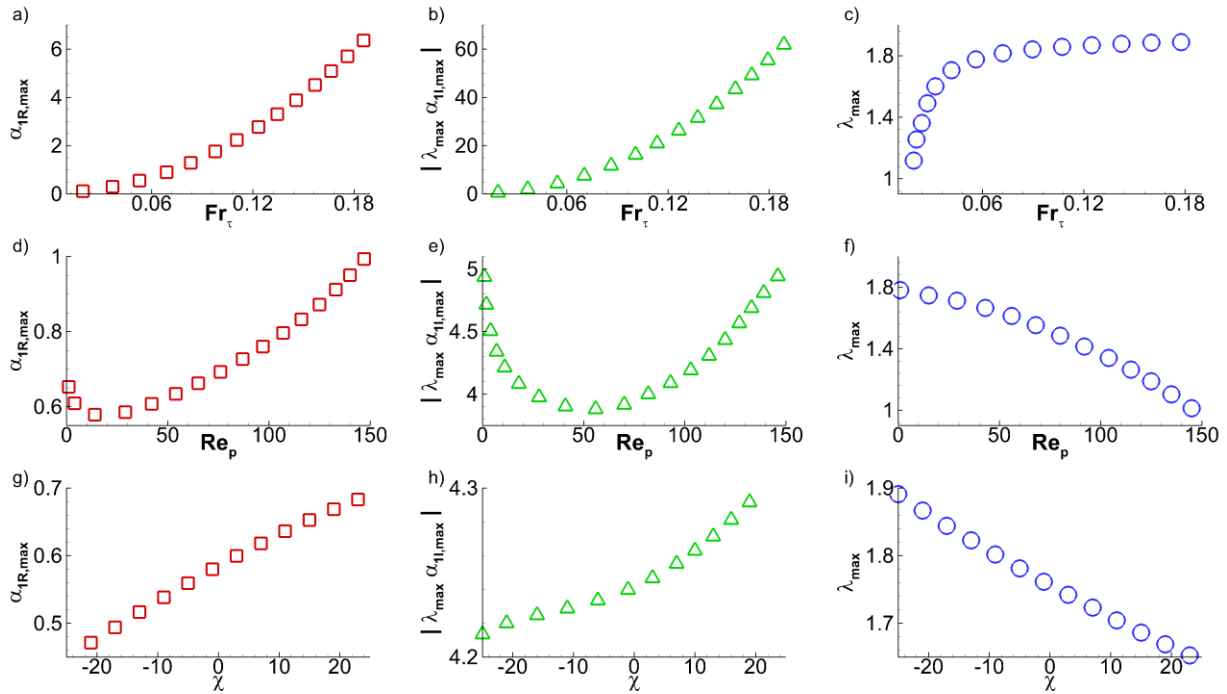

Figure 7. Growth rate, wave speed, and wavelength of most amplified mode versus physical parameters. $Re_p = 1$ and $\chi = 0$ in a) to c), $Fr_\tau = 0.058$ and $\chi = 0$ in d) to f), and $Re_p = 10$ and $Fr_\tau = 0.058$ in g) to i).
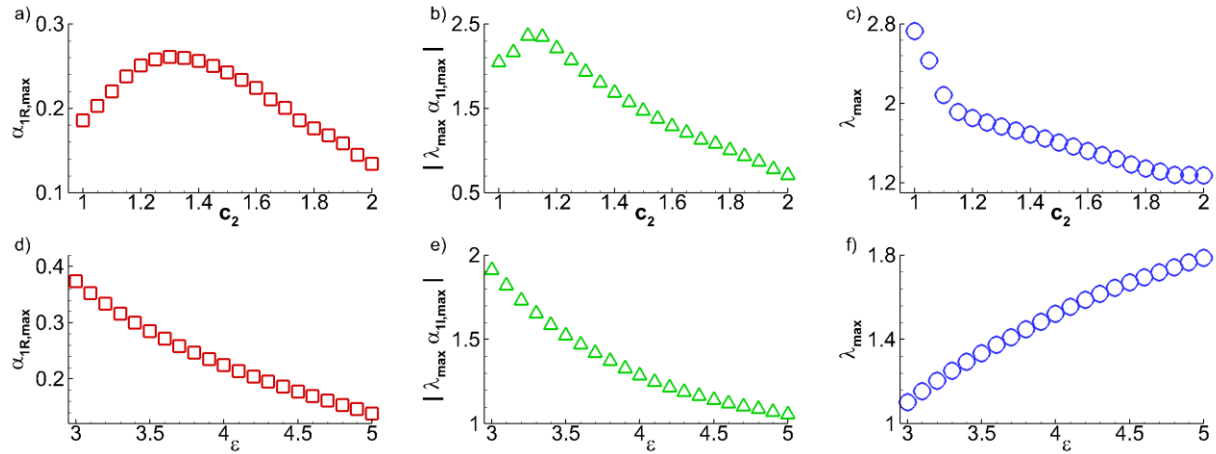
44

Figure 8. Growth rate, wave speed, and wavelength of most amplified mode versus c_2 (ε held fixed at $\varepsilon = 4$) and ε (c_2 held fixed at $c_2 = 1.6$). For all cases, $Re_p = 10$, $Fr_\tau = 0.032$, and $\chi = 0$.
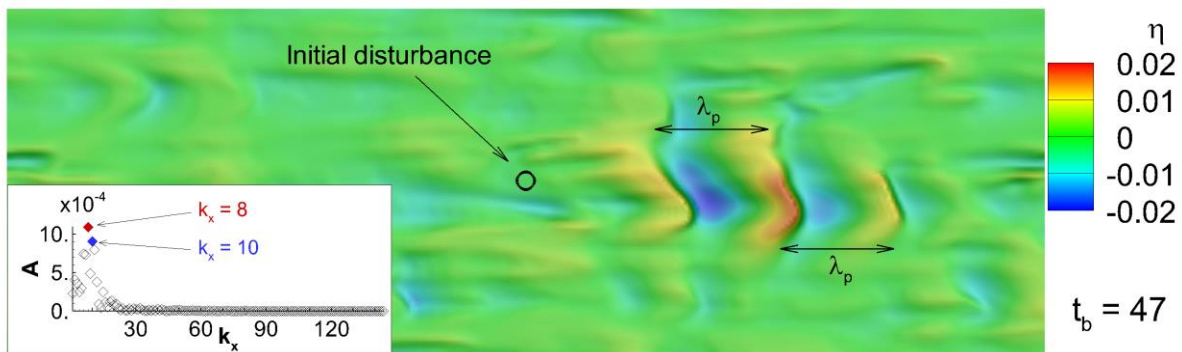

Figure 9. Top view of an erodible bed from Zgheib et al. (2018a) at a time $t_b = 47$ showing three incipient bedforms separated by a distance of λ_p. Contours are for bed elevation η. The bed was perfectly flat except for the presence of a small Gaussian bump whose initial location is marked by the black circle as initial disturbance. Inset) 2-D Fourier decomposition of η provides a quantitative measure for λ_p (see text for details). Flow is from left to right.
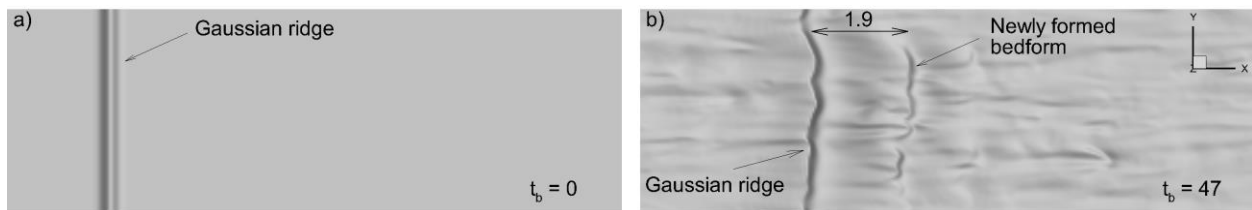

Figure 10. Top view from the Gaussian ridge simulation at a) $t_b = 0$ and b) $t_b = 47$. At $t_b = 0$, the bed is flat except for the presence of the Gaussian ridge. By $t_b = 47$, an incipient bedform has emerged at a distance of approximately 1.9 non-dimensional units from the initial Gaussian ridge. Flow if from left to right.